Energy Conversion and Management 292 (2023) 117376

Contents lists available at ScienceDirect

Energy Conversion and Management

journal homepage: www.elsevier.com/locate/enconman

A big data-handling machine learning model for membrane-based absorber reactors in sorption heat transformers

Mahyar Ashouri [a,1], Naghme Kheyrikoochaksarayee [b,1], Callum Chhokar [a], Amir Shabani [b], Majid Bahrami [a,*]

[a] Laboratory for Alternative Energy Conversion (LAEC), School of Mechatronic Systems Engineering, Simon Fraser University, Canada, and Pacific Institute for Climate Solutions (PICS), Canada

[b] School of Sustainable Energy Engineering, Simon Fraser University, Canada

ARTICLE INFO

Keywords:
Machine learning
Big data
Membrane-based absorbers
Sorption heat transformers
Support vector regression
Random forest regression

ABSTRACT

Membrane-based absorbers have received much attention recently due to their higher absorption rates than conventional absorbers. Several studies have been conducted to analyze membrane-based absorbers' performance using numerical and analytical modeling. Numerical models are accurate; however, they are computationally expensive. Analytical models are computationally efficient; however, they have limiting assumptions and may exhibit inaccuracy accordingly. This study proposes a novel multi-label, big data-handling machine learning model for membrane-based absorbers used in sorption heat transformers, offering the accuracy of a numerical model with the efficient computation of an analytical model. A comprehensive dataset comprising over one million data points is generated using 2D numerical modeling. The dataset consists of 15 features, input parameters, including operating conditions and geometrical parameters, and four labels, output variables, including absorption rate, outlet concentration, solution outlet temperature, and heat transfer fluid outlet temperature. The Support Vector Regression, Random Forest Regression, and Decision Tree Regression are used and combined to develop the present model. Particle swarm optimization is used to find the optimized hyperparameters of each model. A map-reduce algorithm is developed to minimize the computational time, and the optimized data chunk number is presented for the highest accuracy and the lowest computational time. The results of the proposed model are validated with experimental data, capturing most data within a relative difference of 15%. The machine learning-based model can predict the four outputs with an accuracy of over 90%. Moreover, it is shown that using the map-reduce algorithm results in a 40-fold decrease in computation time without significantly compromising accuracy.

1. Introduction

Fossil fuels are the primary source of energy and are one of the main contributors to climate change [1,2]. Heating and cooling are responsible for approximately 80% of the energy consumption in residential buildings [3]. Consequently, considerable attention has been paid to developing sustainable and efficient heating, cooling, and energy storage systems [4]. Currently, most chillers and heat pumps are vapor compression refrigeration systems that run on electricity, mainly generated from burning fossil fuels [5]. Additionally, conventional vapor compression refrigeration systems use ozone-depleting fluorocarbon-type refrigerants [6–8].

Considerable waste heat from various industrial processes is routinely released into the ambient environment [9,10]. About 50% of all primary energy becomes waste heat, with 60% of this waste heat classified as low-grade with a temperature below 100 °C [11]. Recovering, storing, and converting low-grade waste heat can reduce greenhouse gas emissions significantly. Such systems are the topic of many exploratory studies [12]. Heat-driven absorption heat transformers, chillers/heat pumps, are one such system. Absorption heat transformers use low-grade heat and ozone-friendly working fluids [13–15]. However, existing absorption heat transformers are not economically viable since they suffer from a low Coefficient of Performance (COP).

The absorber and its absorption rate dictate absorption heat transformers' cost and performance. High absorption rates often require an

* Corresponding author.
E-mail address: mbahrami@sfu.ca (M. Bahrami).
[1] Both authors contributed equally to this work.

https://doi.org/10.1016/j.enconman.2023.117376
Received 2 May 2023; Received in revised form 3 July 2023; Accepted 4 July 2023
Available online 7 July 2023

Nomenclature

A_c	Channel cross-section area, m^2
C	Concentration of absorbate, kg kg^{-1}
c	Isobaric specific heat, $J{\cdot}kg^{-1}$ K^{-1}
D	Mass diffusivity, $m^2{\cdot}s^{-1}$
D_m	Membrane mean pore diameter, μm
g	Gravity, $m{\cdot}s^{-2}$
h_{abs}	Absorption heat, J kg^{-1}
J	Mass flux, kg m^{-2} s^{-1}
k_m	Membrane mass transfer coefficient, kg m^{-2} s^{-1} Pa^{-1}
p	Pressure, Pa
L_m	Membrane length, m
M	Molecular mass, g mol^{-1}
$\dot{m}$	Mass flux, kg m^{-2} s^{-1}
$\dot{q}$	Heat flux, W m^{-2}
R	Universal gas constant, J/mol^{-1} K^{-1}
T	Temperature, K
$\bar{u}$	Average velocity, m s^{-1}
x, y	Local tangential and normal position, m

Greek symbols

α	Thermal diffusivity, m^2 s^{-1}
φ	Membrane porosity
τ	Membrane tortuosity
δ	Film thickness, μm
ρ	Density, kg m^{-3}

Subscripts

HX	Heat exchanger
HTF	Heat transfer fluid
m	Membrane
in	Inlet
inf	Interface
s	Solution
v	Vapor
w	Wall

Abbreviations

COP	Coefficient of Performance
CFD	Computational fluid dynamics
DTR	Decision tree regression
RFR	Random forest regression
SVR	Support vector regression
MSE	Mean squared error
RMSE	Root mean squared error

oversized heat and mass exchanger [16]. Several configurations have been suggested to improve the performance and reduce the cost of the absorber; these include: i) laminar and turbulent falling films, ii) bubbly flows, and iii) the use of atomizers [17]. While only marginally enhancing the absorption rate, these designs lead to inefficient, heavy, and complex absorbers. These absorbers have three main issues: high film thickness, flow separation, and a low surface-wetting ratio. Recently, membrane-based absorbers have become popular for their ability to enhance the COP of absorption chillers/heat pumps [18–24]. A microporous/nanofibrous membrane separates the liquid and vapor phases in this absorber type. The liquid phase cannot go through the selective membrane, while the vapor phase can, leading to vapor absorption.

Membrane-based absorbers have been modeled theoretically, analytically, and numerically. Ali [25] developed a theoretical model to design a compact membrane-based absorber with a hydrophobic microporous membrane. Ashouri and Bahrami [26] proposed two analytical solutions for membrane-based absorbers using the Laplace transform method [27] and similarity solution [28].

Yu et al. [29] performed a parametric study on a membrane-based absorber using the Lattice Boltzmann method. A comprehensive parametric study was performed to quantify the influence of different operational and geometrical parameters. They reported that the solution film thickness and velocity were the key parameters. Asfand et al. [30] performed a 3D CFD simulation to calculate the heat and mass transfer in a membrane-based absorber. They showed a three-fold enhancement in absorption rate could be acquired by decreasing the thickness of the solution channel from 2 mm to 0.5 mm. Venegas et al. [17] proposed a 1D numerical model, developed based on a mass transfer resistance network, for a membrane-based absorber, and validated the model with experimental data available in the literature.

Several other studies have been conducted to analyze membrane-based absorber performance using computational fluid dynamics and numerical methods [31–34]. These methods can produce detailed, accurate results; however, implementing them incurs a high computational cost. Although they offer efficient computation, membrane-based absorber analytical models have many limiting assumptions, constraining their applicability and presenting inaccuracies. These models consider isothermal boundary conditions at the heat exchanger wall and, as such, cannot consider temperature lift and heat exchanger wall thickness [26].

Machine learning is an emerging tool that provides the accuracy of a numerical model and the time efficiency of an analytical model. There are only a few studies on membrane-based absorbers that use machine learning. Sui et al. [35] developed a three-dimensional CFD model to investigate a membrane-based absorber with inclined grooves on the heat exchanger wall. A machine learning method based on an artificial neural network and non-dominated sorting genetic algorithm-II was developed to optimize the grooves' geometries and maximize the integrated performance. In addition to geometric optimization, Sui et al. [36] used eight different types of machine learning algorithms: K-nearest neighbor, support vector machines, extra tree, decision tree, backpropagation neural networks, extreme gradient boosting, partial least squares, and random forest to find the best ionic liquid absorbent candidate. Sui and Wu [37] also developed an Artificial Intelligence model to minimize flow maldistribution in membrane-based absorbers.

For the first time, this study proposes a novel multi-label, big data-handling machine learning model to predict the heat and mass transfer in membrane-based absorbers used in absorption chillers and heat pumps. A comprehensive dataset, comprising one million data points, is generated using 2D numerical modeling using the Compute Canada supercomputers, namely, Narval, Cedar, Graham, and Beluga [34]. The dataset consists of 15 features, input parameters, including operating conditions and geometrical parameters, and four labels, output variables, including absorption rate, outlet concentration, solution outlet temperature, and heat transfer fluid outlet temperature. The Support Vector Regression, Random Forest Regression, and Decision Tree Regression are used and combined to develop the present model. The particle swarm optimization is used to find the optimized hyperparameters of each model. A map-reduce algorithm is developed to minimize the computational time, and the optimized data chunk number is presented for the highest accuracy and the lowest computational time. The results of the machine learning-based model are validated with experimental data available in the literature. The developed machine learning-based model (source code) and the dataset are shared on the authors' GitHub and are provided as supplementary material, enabling prospective readers to perform membrane-based absorber design, real-time control, and optimization in an accurate, time-efficient

manner. Also, the present big data-handling machine learning model, developed based on a customized MapReduce algorithm, can be used for other multi-label regression problems by only changing the name of features and labels in the present source code.

2. Problem description and formulation of assumptions

Coupled heat and mass transfer in membrane-based absorbers is numerically studied for single and double-sided configurations, as schematically shown in Fig. 1. Aqueous LiBr, which is the most common absorbent in absorption chillers and heat pumps, is used as the absorbent. The aqueous LiBr is mechanically constrained via a hydrophobic nanofibrous, microporous membrane and a heat exchanger wall to adjust the film thickness. The membrane is hydrophobic, thus it is impermeable to the aqueous LiBr solution, while water vapor can pass through it. Since the water vapor partial pressure at the solution-membrane interface is less than the vapor pressure, the water vapor traverses the membrane and is absorbed at the solution-membrane interface, diffusing into the bulk of the aqueous LiBr. Absorption is an exothermic process, therefore; the temperature of the aqueous LiBr increases due to the heat of absorption, leading to a decrease in the absorption rate due to variation in the solution equilibrium concentration, if the solution temperature is not maintained through cooling. Therefore, the temperature of the aqueous LiBr is maintained using a heat exchanger.

The following assumptions have been made to develop the proposed analytical model [38]:

- The system works under a steady-state condition;
- The flow is laminar (the Reynolds number, $Re < 6$) and hydrodynamically fully developed (development length, $L_{development} = 0.0575{*}Re{*}D < 0.4mm$ [39], where D is hydraulic diameter);
- The absorbent is non-volatile;
- The heat transfer from the absorbent to the membrane is neglected. The membrane is thin (~100 μm), and highly porous (~90%); therefore, its sensible heat storage is negligible considering its low mass [30,40];
- The heat transfer from the absorbent to the water vapor is negligible since the system works under a vacuum condition;
- Membrane is hydrophobic in this application; thus the solution does not penetrate the membrane [30,40];
- Concentration and temperature distributions are uniform and constant at the inlet; and
- The membrane's mean temperature is constant (see Ref. [38] for more details).

3. Model development

3.1. Governing equations

The solution velocity for the flow between two the membrane and heat exchanger wall is as follows:

$$u_s = 6\overline{u}_s\left(\frac{y_s}{\delta_s} - \left(\frac{y_s}{\delta_s}\right)^2\right) \tag{1}$$

where u_s, $\overline{u}_s$, and δ_s are the solution velocity, the solution mean velocity, and the solution thickness, respectively. The heat transfer fluid velocity for the flow within the heat transfer fluid channel is as follows:

$$u_{HTF} = 6\,\overline{u}_{HTF}\left(\frac{y_{HTF}}{\delta_{HTF}} - \left(\frac{y_{HTF}}{\delta_{HTF}}\right)^2\right) \text{one} - \text{sided} \tag{2}$$

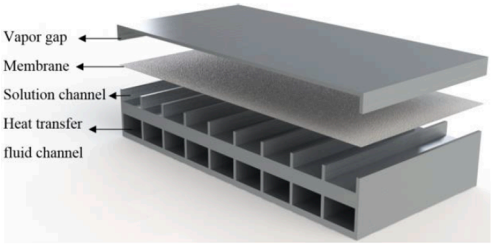

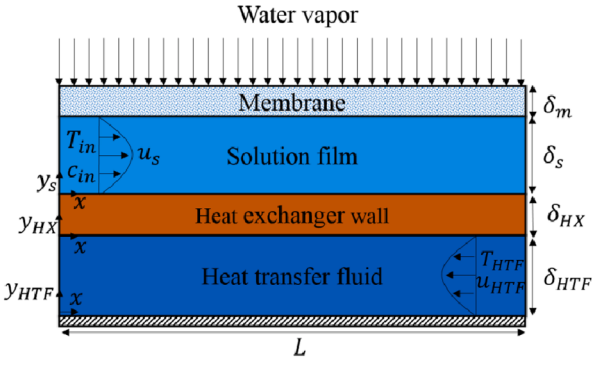

(a)

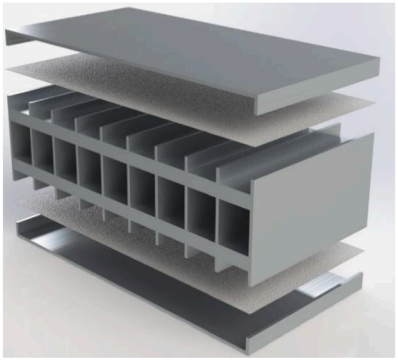

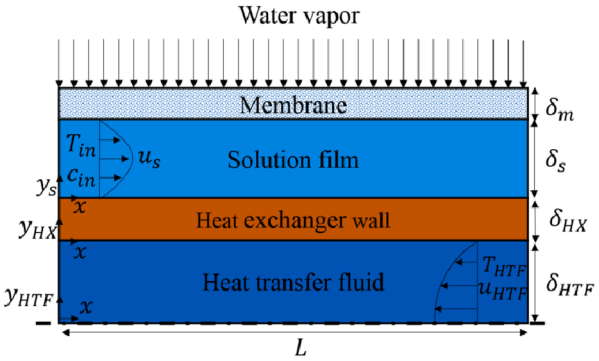

(b)

Fig. 1. Schematic diagram of membrane-based absorber over a heat exchanger. (a) single-sided configuration, and (b) double-sided configuration.

$$u_{HTF} = 1.5\,\bar{u}_{HTF}\left(1 - \left(\frac{y_{HTF}}{\delta_{HTF}}\right)^2\right) \text{ double} - \text{sided} \tag{3}$$

where u_{HTF}, $\bar{u}_{HTF}$, and δ_{HTF} are the heat transfer fluid velocity, the heat transfer fluid mean velocity, and the heat transfer fluid thickness, respectively. Given the advective transport in the flow direction "x_s" and the diffusivity transport in the normal direction "y_s" for the solution domain, the following governing equations for energy and species conservation can be derived, respectively:

$$u_s \frac{\partial T_s}{\partial x} = \alpha_s \frac{\partial^2 T_s}{\partial y_s^2} \tag{4}$$

$$u_s \frac{\partial c}{\partial x} = D_s \frac{\partial^2 c}{\partial y_s^2} \tag{5}$$

where T, α_s, and D_s are the solution's temperature, thermal diffusivity, and mass diffusivity, respectively. It should be mentioned that "c" is the water (absorbate) concentration (kg water/kg solution), not the solution concentration (kg LiBr/kg solution). Energy equations for the heat transfer fluid and heat exchanger wall can be written as follows:

$$u_{HTF} \frac{\partial T_{HTF}}{\partial x} = \alpha_{HTF} \frac{\partial^2 T_{HTF}}{\partial y_{HTF}^2} \tag{6}$$

$$\frac{\partial^2 T_{HX}}{\partial y_{HX}^2} + \frac{\partial^2 T_{HX}}{\partial x^2} = 0 \tag{7}$$

where T_{HTF}, α_{HTF}, and T_{HX} are the heat transfer fluid's temperature, thermal diffusivity, and heat exchanger's temperature, respectively. The Dusty-Gas model [41] is used to model the mass transfer through the membrane. This mass transfer includes molar diffusion and viscous fluxes, which can be calculated as follows [29]:

$$J = k_m(p_v - p_{inf}) \quad \left[\frac{kg}{m^2.s}\right] \tag{8}$$

where k_m, p_v, and p_{inf} are the membrane mass transfer coefficient, vapor pressure, and water vapor partial pressure at the membrane-solution interface, respectively. The membrane mass transfer coefficient can be found as follows [29]:

$$k_m = -\frac{\varphi D_m}{\delta_m \tau}\left(\sqrt{\frac{8M}{9\pi R T_m}} + \frac{p_v D_m}{32 \mu_g R T_m}\right) \quad \left[\frac{kg}{Pa.m^2.s}\right] \tag{9a}$$

$$T_m = \frac{T_{s-in} + T_{HTF} + T_v}{3} \quad [K] \tag{9b}$$

$$\tau = \frac{(2-\varphi)^2}{\varphi} \tag{9c}$$

where φ, D_m, τ, δ_m, and R are the membrane porosity, mean pore diameter, tortuosity, thickness, and the universal gas constant, respectively. In addition, M, μ_g, and T_m are the water vapor molar weight and dynamic viscosity, and average membrane temperature, respectively. The average membrane temperature is assumed to be an average of the inlet solution temperature "T_{s-in}", inlet heat transfer fluid temperature "T_{HTF}", and water vapor temperature "T_v" [38].

3.2. Boundary conditions and modeling procedures

The boundary conditions for the solution, heat exchanger, and heat transfer fluid are as follows [27]:

$$T_s(x=0, y_s) = T_{s-in} \;\&\; c\,(x=0, y_s) = c_{in} \tag{10}$$

$$\rho_s D_s \left.\frac{\partial c}{\partial y_s}\right|_{inf} = k_m(p_v - p_{inf}) \tag{11}$$

$$-k_s \left.\frac{\partial T_s}{\partial y_s}\right|_{inf} = h_{abs} k_m (p_v - p_{inf}) \tag{12}$$

$$-k_s \left.\frac{\partial T_s}{\partial y_s}\right|_{y_s=0} = -k_{HX} \left.\frac{\partial T_{HX}}{\partial y_{HX}}\right|_{y_{HX}=\delta_{HX}} \tag{13}$$

$$\left.\frac{\partial T_{HX}}{\partial x}\right|_{x=0} = \left.\frac{\partial T_{HX}}{\partial x}\right|_{x=L} = 0 \tag{14}$$

$$-k_{HX} \left.\frac{\partial T_{HX}}{\partial y_{HX}}\right|_{y_{HX}=0} = -k_{HTF} \left.\frac{\partial T_{HTF}}{\partial y_{HTF}}\right|_{y_{HTF}=\delta_{HTF}} \tag{15}$$

$$T_{HTF}(x=L, y_{HTF}) = T_{HTF} \text{ counter flow} \tag{16}$$

$$T_{HTF}(x=0, y_{HTF}) = T_{HTF} \text{ parallel flow} \tag{17}$$

$$\left.\frac{\partial T_{HTF}}{\partial y_{HTF}}\right|_{y_{HTF}=0} = 0 \tag{18}$$

The water vapor partial pressure at the membrane-solution interface "p_{inf}" for the LiBr-water solution can be calculated based on the following experimental correlation [13]:

$$p_{inf}(T_{s-inf}, c_{inf}) = \exp\left(A + \frac{B}{T_{inf}} + \frac{C}{T_{inf}^2}\right) \tag{19a}$$

$$A = a_1 + a_2 c_{s,inf} + a_3 c_{s,inf}^2 \tag{19b}$$

$$B = a_4 + a_5 c_{s,inf} + a_6 c_{s,inf}^2 \tag{19c}$$

$$C = a_7 + a_8 c_{s,inf} + a_9 c_{s,inf}^2 \tag{19d}$$

where the corresponding constants can be found in Ref. [13]. The heat and mass transfer rates can be found as follows:

$$\dot{q}(x) = -k_s \left.\frac{\partial T_s}{\partial y_s}\right|_{inf} \quad \left[\frac{w}{m^2}\right] \tag{20}$$

$$\dot{m}(x) = \rho_s D_s \left.\frac{\partial c}{\partial y_s}\right|_{inf} \quad \left[\frac{kg}{m^2 s}\right] \tag{21}$$

The governing equations (Eqs (4–7)) should be solved simultaneously. In this study, the finite difference method was used. The first and second derivatives of parameters were discretized using the central difference method. Virtual nodes were considered to couple the boundary conditions to the domain to maintain the second-order accuracy for the solution. All the equations were solved iteratively until a residual of 10^{-8} was reached for each parameter. Thermophysical properties for the solution and the heat transfer fluid were calculated at each iteration. These properties can be found in Ref [42]. The numerical model was coded in MATLAB software. Computations were performed on Compute Canada supercomputers, namely, Narval, Cedar, Graham, and Beluga [43].

3.3. Mesh independency study

Several different values for $\Delta x, \Delta y_s, \Delta y_{HX}$, and Δy_{HTF} were studied to ensure mesh independency. Since the mesh is conformal, Δx was the same for the solution heat exchanger and heat transfer fluid domains. Table 1 shows the parameters of the investigated case for the mesh independence study. Outlet solution concentration and heat transfer fluid temperature were considered as the criteria. Fig. 2 shows the variation in the outlet solution concentration and heat transfer fluid temperature

Table 1
Considered parameters for the mesh independency study.

Parameter	Value	Parameter	Value
Absorber length $L[m]$	0.05	Heat exchanger wall thickness $\delta_{HX}[mm]$	3
Solution thickness $\delta_s[\mu m]$	500	Heat transfer fluid thickness $\delta_{HTF}[mm]$	2
Average solution velocity $\overline{u}_s\left[\frac{mm}{s}\right]$	10	Heat exchanger thermal conductivity $k_{HX}\left[\frac{W}{m.K}\right]$	16
Solution inlet temperature $T_{s-in}[^\circ C]$	40	Average heat transfer fluid velocity $\overline{u}_{HTF}\left[\frac{mm}{s}\right]$	2
Water inlet concentration $c_{in}\left[\frac{kg\ water}{kg\ solution}\right]$*	0.4	Configuration	Single-sided
Heat transfer fluid inlet temperature $T_{HTF}[^\circ C]$	30	Mesh number 1: $\Delta x = 5mm$, $\Delta y_s = 5\mu m, \Delta y_{HX} = 1mm$, and $\Delta y_{HTF} = 100\mu m$	1000
Vapor pressure $p_v[kPa]$	1740	Mesh number 1: $\Delta x = 3.75mm$, $\Delta y_s = 3.75\mu m, \Delta y_{HX} = 750\mu m$, and $\Delta y_{HTF} = 75\mu m$	2000
Membrane porosity φ	0.8	Mesh number 1: $\Delta x = 2.5mm$, $\Delta y_s = 2.5\mu m, \Delta y_{HX} = 500\mu m$, and $\Delta y_{HTF} = 50\mu m$	4500
Membrane pore diameter $D_m[\mu m]$	0.5	Mesh number 1: $\Delta x = 1.25mm$, $\Delta y_s = 1.25\mu m, \Delta y_{HX} = 250\mu m$, and $\Delta y_{HTF} = 25\mu m$	2000
Membrane thickness $\delta_m[\mu m]$	50	Mesh number 1: $\Delta x = 0.5mm$, $\Delta y_s = 0.5\mu m, \Delta y_{HX} = 100\mu m$, and $\Delta y_{HTF} = 10\mu m$	120,000

* Water concentration $c_o = 1 - X$ where X is solution concentration.

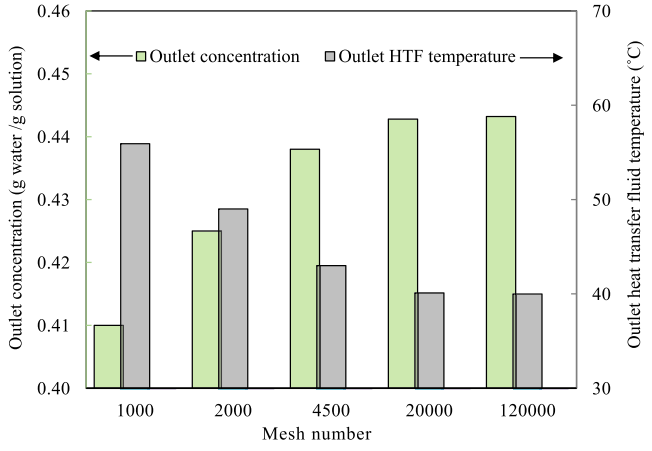

Fig. 2. Variation in the outlet solution concentration and outlet heat transfer fluid temperature versus different mesh numbers.

versus different mesh numbers. As seen in Fig. 2, a 120,000 mesh number was sufficient for mesh independency. $\Delta x = 500\mu m$, $\Delta y_s = 0.5\mu m, \Delta y_{HX} = 100\mu m$, and $\Delta y_{HTF} = 10\mu m$ were used for all other cases since variations in the outlet solution concentration and outlet heat transfer fluid temperature were negligible with increasing mesh number.

4. Data analytic pipeline

In this section, different components of the data analytic pipeline including data description, data processing, and machine learning models are explained.

4.1. Data description

For this study, we generated a big dataset, which comprises one million data, using a 2D numerical model of a membrane-based absorber. The dataset includes 15 features, input parameters, including operating conditions and geometrical parameters. The range of these features is presented in Table 2, and Fig. 3 shows their value distribution. To make sure the features' ranges are realistic, we used all practical ranges by considering the operating conditions and geometrical parameters of actual setups available in the literature [44–47] and the physics of phenomena occurring in membrane-based absorbers.

All features were generated using uniform distribution to prevent bias in the dataset. However, the distribution of some features, as shown in Fig. 3, was not uniform. The reason is that some conditions could not fulfill the numerical modeling. For instance, absorption does not occur when the solution inlet concentration is 0.5 and the vapor pressure is 870 Pa since the water vapor partial pressure at the membrane-solution interface is greater than the vapor pressure. Therefore, many data points were intuitively eliminated based on the physics of the phenomena.

Table 2
List of features (inputs) and their range used in generating the dataset.

Feature name	Feature type	Feature range	Available experimental range in the literature [44–47]
Absorber length $L[cm]$	Numeric	1 –10	3 –5
Solution thickness $\delta_s[\mu m]$	Numeric	50 –500	100 –200
Average solution velocity $\overline{u}_s\left[\frac{mm}{s}\right]$	Numeric	0.1 –20	5 –15
Solution inlet temperature $T_{s-in}[^\circ C]$	Numeric	25 –55	25 –35
Water inlet concentration $c_{in}\left[\frac{kg\ water}{kg\ solution}\right]$*	Numeric	0.38 –0.55	0.4 –0.45
Heat transfer fluid inlet temperature $T_{HTF}[^\circ C]$	Numeric	25 –55	25 –30
Vapor pressure $p_v[kPa]$	Numeric	0.840 –2.34	0.840 –1.9
Membrane porosity φ	Numeric	0.1 –1	0.4 –0.9
Membrane pore diameter $D_m[\mu m]$	Numeric	0.2 –3	0.45 –1
Membrane thickness $\delta_m[\mu m]$	Numeric	10 –250	50 –150
Heat exchanger wall thickness $\delta_{HX}[mm]$	Numeric	0.5 –5	N/A
Heat transfer fluid thickness $\delta_{HTF}[mm]$	Numeric	0.25 –5	0.25 –5
Heat exchanger thermal conductivity $k_{HX}\left[\frac{W}{m.K}\right]$	Numeric	13–17 Stainless steel 170–230 Aluminum	Both
Average heat transfer fluid velocity $\overline{u}_{HTF}\left[\frac{mm}{s}\right]$	Numeric	0.1 –20Parallel flow −0.1*to* −20Counter flow	N/A
Configuration	Binary	0 single-sided configuration 1 double-sided configuration	Single-sided configuration

* Water concentration $c_o = 1 - X$ where X is solution concentration.

The four labels, the output variables of the system, are absorption rate, solution outlet concentration, solution outlet temperature, and heat transfer fluid outlet temperature. While three of these output variables are independent, the absorption rate can be calculated using outlet solution concentration:

$$\dot{m}_{ave} = \frac{\rho_s(T_o, c_o)\,\overline{u}_s\,\delta_s}{L}\,(c_{out} - c_{in}) \quad [\frac{kg}{m^2 s}] \tag{22}$$

4.2. Machine learning-based model development

Considering the four continuous output variables of the systems, the problem in hand is a multi-variate regression. Several different linear or nonlinear regression models in machine learning (ML) literature were used to learn the core characteristics of the underlying physical system using the synthetic dataset [48–55]. However, without any information on whether the data is structured or semi-structured, a nonlinear model such as the Support Vector Regression (SVR) should work better than a linear regression model such as the logistic regression [56]. SVR handles unstructured or semi-structured data well while identifying the nonlinear relationships between variables and providing flexibility to adjust the model's robustness by tuning hyper-parameters [57]. It is also well known that in contrast to a single model, ensemble methods that use the fusion of multiple models can provide higher performance while improving robustness by reducing the spread or dispersion of the predictions. Among different ensemble techniques, Random Forest Regression (RFR) and Decision Tree Regression (DTR) have shown decent performance in different applications [58,59].

During the development of the present model, we observed an inconsistency in the range of output variables. In fact, the range is very large for some variables while it is too small for some other variables. This inconsistency in the range reduces the accuracy of both the SVR and RFR. To compensate for this inconsistency, a common practice is an

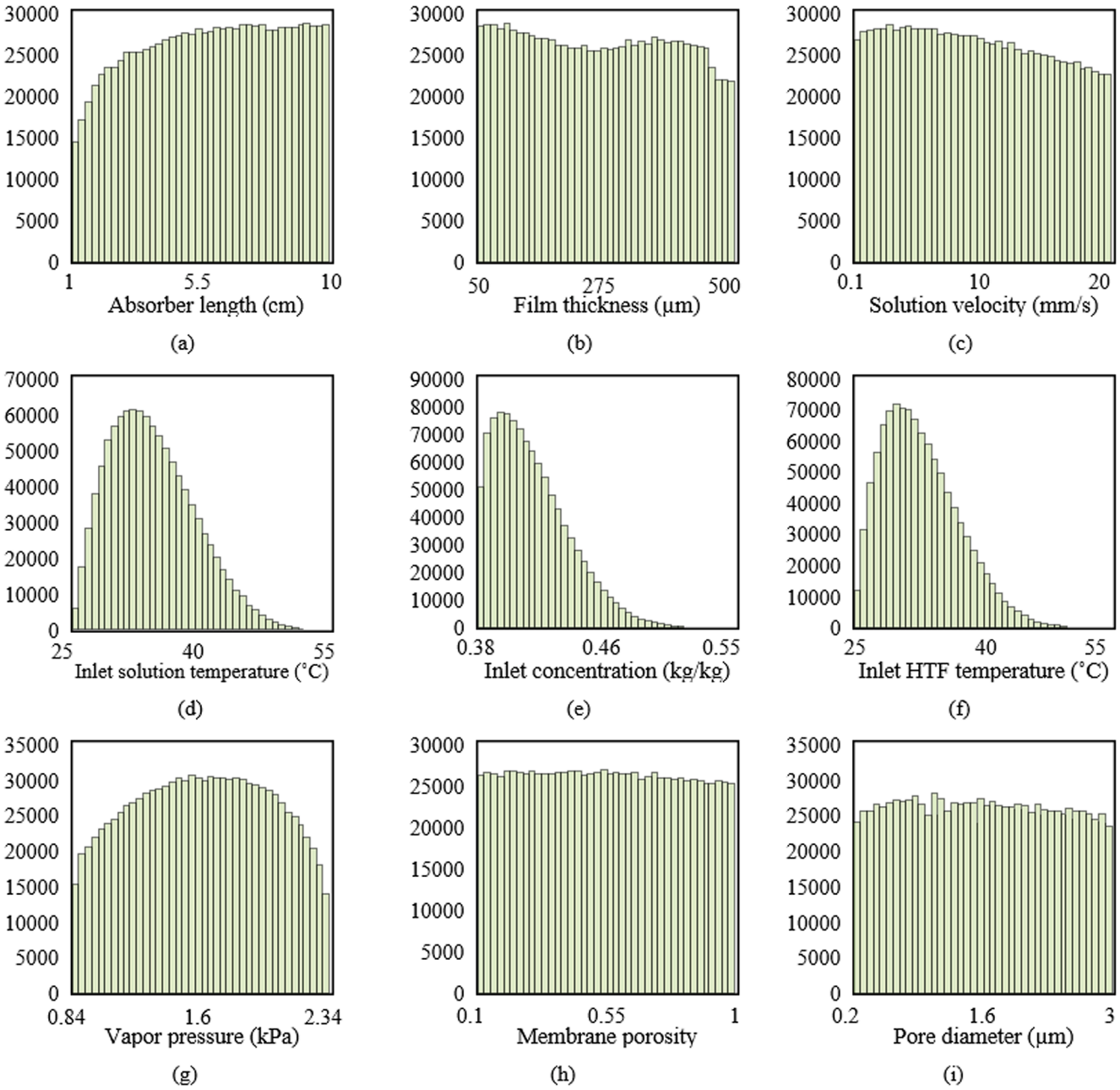

Fig. 3. Distribution of features (inputs) (a) to (o) and independent labels (outputs) (p) to (r) over their corresponding ranges.

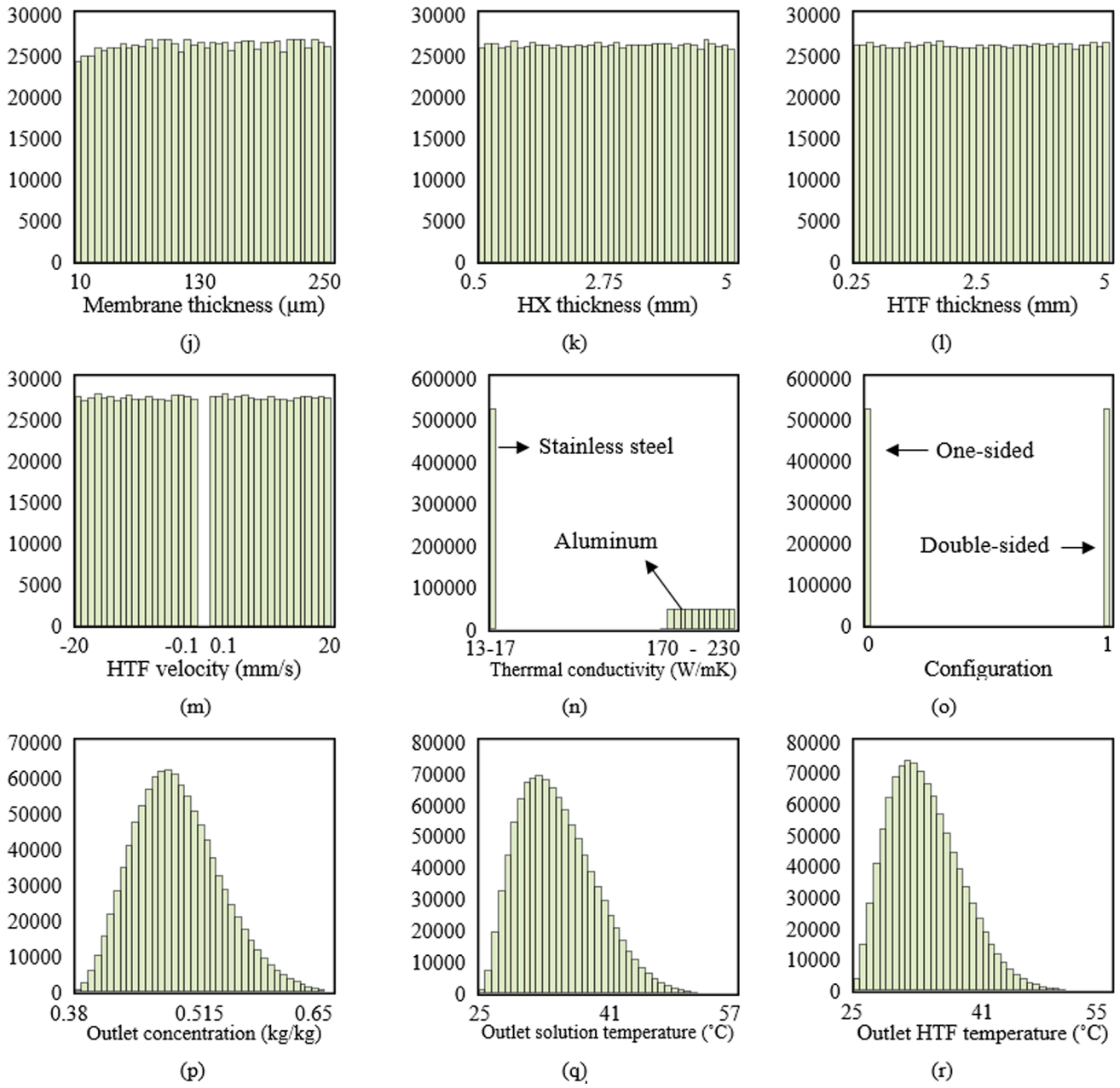

Fig. 3. (*continued*).

auto-scale adjustment through which output variables will be mapped to a new space in which there is a reasonable range for each variable. After prediction, the inverse of the mapping is applied to the variables to be converted back to the real space. Table 3 provides the details of this mapping and inverse scaling.

The whole point of generating a very large dataset was to make sure all possible realistic ranges for input variables are covered, however, with an increase in the number of input data points, we observed a significant increase in the computational complexity of the regression models, especially SVR and RFR. We also observed that these models perform differently for a different portion of the features' range, leading us to believe that not a single regressor will perform the best and hence a fusion of regressors should be used. Moreover, to address the challenges of the computation cost, similar to any big data analytics problem, the Map-Reduce paradigm [60] should remedy the situation as it enables the processing of such a large dataset in a parallel manner. To ensure the stability and robustness of the final model while achieving a decent accuracy with the MapReduce approach, we used both bagging ensembles and stacking ensembles and hence a fusion of SVR, RFR, and DTR regressors. To be more specific, the split of datasets into several chunks provides the benefit of bagging while fusing the trained regression models on those chunks to finalize the prediction for the whole dataset resembles the stacking ensembles.

Fig. 4 provides an infographic representation of the training and testing phase of the ML framework within the MapReduce paradigm. First, 90% of the entire dataset is randomly selected as the training dataset for the map phase, and 10% of the entire data set is used as the testing dataset for the reduce phase, as shown in Fig. 4 (a). The training dataset is then divided into ″m″ data chunks. Each data chunk is again divided into a 90% training set and a 10% validation set. The training set is then used to train SVR, RFR, and DTR, and the validation set is used to evaluate the models and assign a normalized weight to each model. A similar procedure is repeated for all ″m″ data chunks. Fig. 4 (b) shows the reduce phase when the entire training dataset is fed to all of the

Table 3
Procedure of mapping data before training and the inverse of mapped predicted labels.

Label	Mapping of the input labels	Inversing of predicted labels
Outlet concentration	$c_{out-mapped} = 30(c_{out-real} - c_{in})^{0.2}$	$c_{out-predicted-real} = \left(\frac{c_{out-pridicted}}{30}\right)^{5} + c_{in}$
Solution outlet temperature	$T_{s-out-mapped} = 100(T_{out-real} - T_{s-in})$	$T_{out-predicted-real} = \frac{T_{out-pridicted}}{100} + T_{s-in}$
Heat transfer fluid outlet temperature	$T_{HTF-out-mapped} = 10000(T_{HTF-out-real} - T_{HTF-in})$	$T_{HTF-out-predicted-real} = \frac{T_{HTF-out-pridicted}}{10000} + T_{HTF-in}$

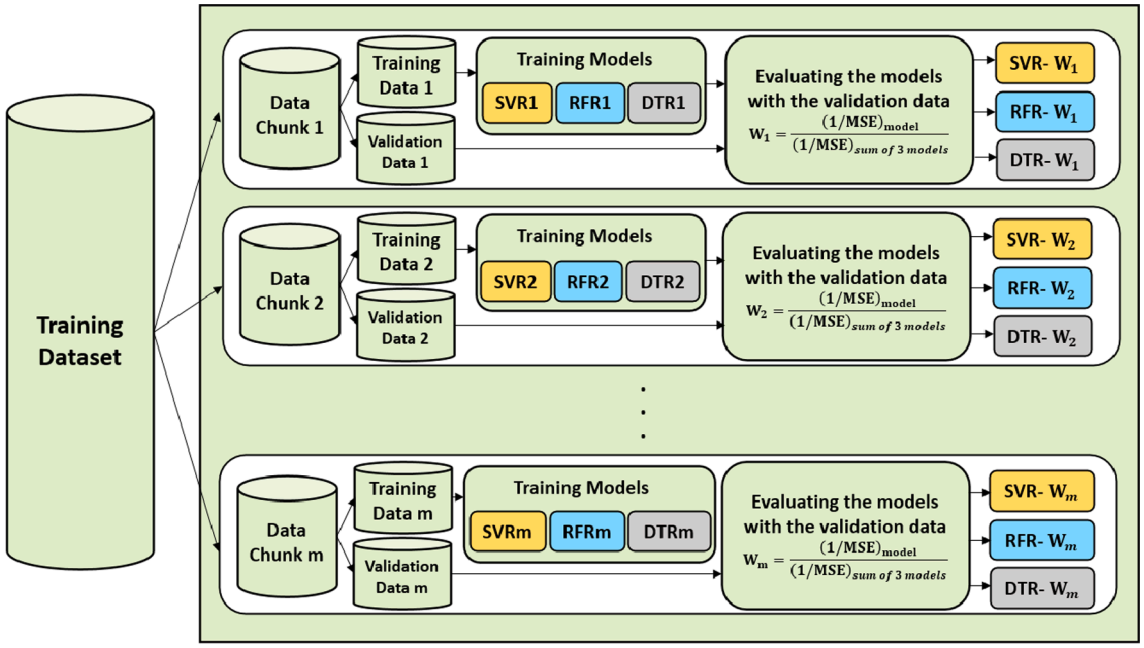

(a)

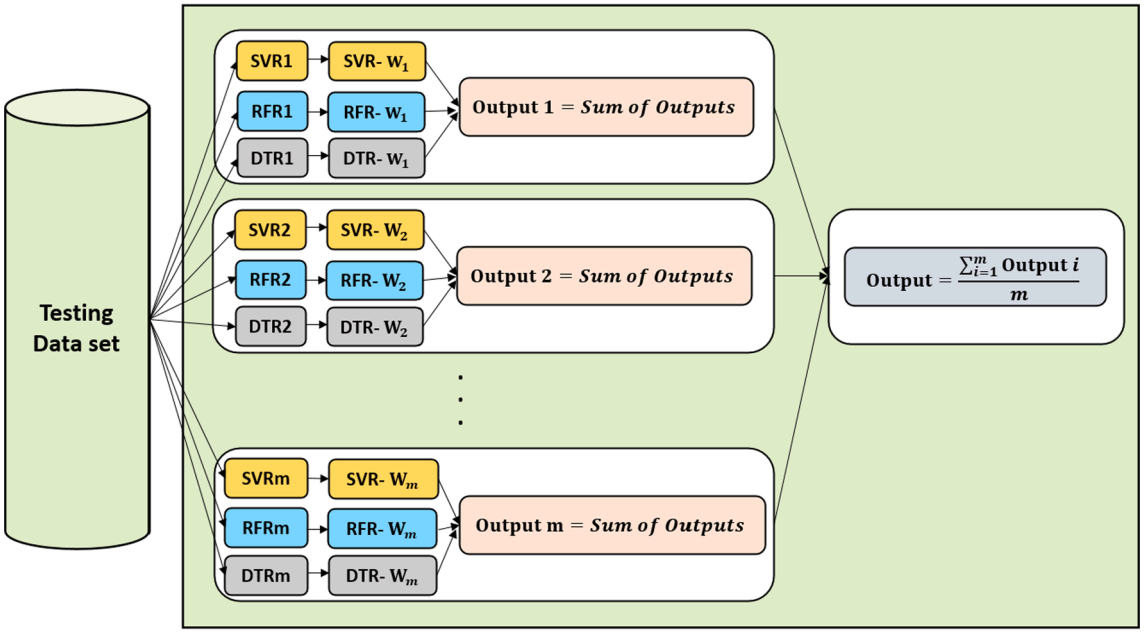

(b)

Fig. 4. Infographic representation of the map-reduce approach in handling our very large dataset during (a) training (map phase) and (b) testing (reduce phase).

trained SVRs, RFRs, and DTRs. The output of each model is multiplied by the corresponding normalized weight. The summation of all the outputs contributions is divided by "m" to predict the final value for each of the four output variables. To find the optimized hyperparameters of each model, we used the stochastic optimization method of Particle Swarm [61] as the given vector space is multi-dimensional.

To provide a greater access of the experimentation to the public, the model and the dataset will be available on the author's GitHub (and as supplementary data to this paper), enabling prospective readers to perform real-time absorber control, optimization, and design in an accurate, time-efficient manner.

5. Results and discussion

5.1. Effect of data number, chunk number, and combination of SVR, RFR, and DTR on accuracy

The present dataset is completely balanced; the distribution of all features is the same for each desired pressure range. Therefore, a pressure range of 1200 to 1270 Pa, which includes 50,000 instances, is used to investigate the effect of instances, chunk number, and combining SVR, RFR, and DTR on the model accuracy. Root Mean Square Error (RMSE) is used as the criteria to measure accuracy. For SVR, C = 10, epsilon = 0.1, and RBF kernel are used. For RFR, a maximum number of estimators of 200 and a depth of 50 are used. A depth of 1000 is used for DTR. Fig. 5 shows the effect of data number (number of instances) on RMSE for four labels: absorption rate, outlet concentration, solution outlet temperature, and heat transfer fluid outlet temperature. The following can be observed:

i) RMSE decreases by increasing the number of data.
ii) By comparing the RMSE of 25,000 and 50,000 cases, it is deduced that 50,000 data can be enough to predict all the labels. Since the dataset is balanced, this conclusion can be applied to any desired pressure range (some other ranges were tested but not reported here).
iii) Absorption rate is the most challenging label to predict since its range is very low ($\sim 10^{-5}$ – 0.025, see Figs. 9 and 10).

Fig. 6 shows the effect of chunk number on the computation time and RMSE for the present labels (output variables) including absorption rate, outlet concentration, solution outlet temperature, and heat transfer fluid outlet temperature. It should be noted that the RMSE and run-time are the average of 5 runs for each case. The following can be observed:

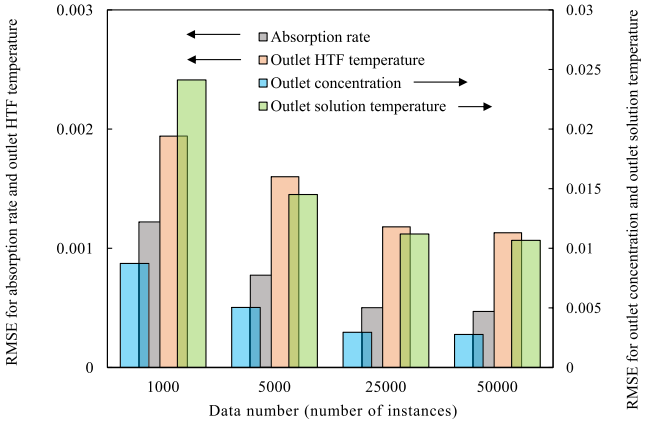

Fig. 5. Effect of data number on RMSE for the present labels: absorption rate, outlet concentration, solution outlet temperature, and heat transfer fluid outlet temperature.

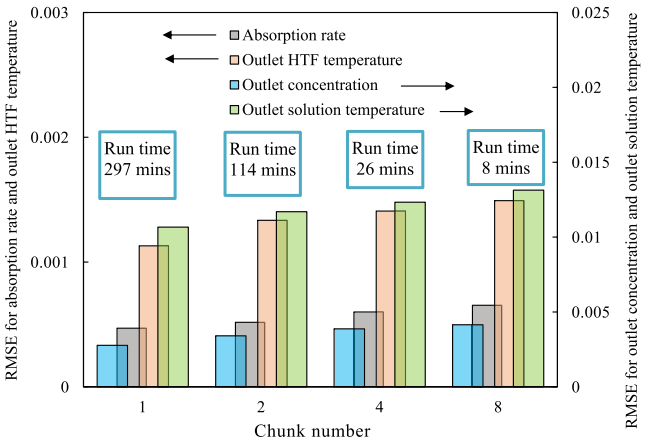

Fig. 6. Effect of chunk number on RMSE and computational time for the present labels: absorption rate, outlet concentration, solution outlet temperature, and heat transfer fluid outlet temperature.

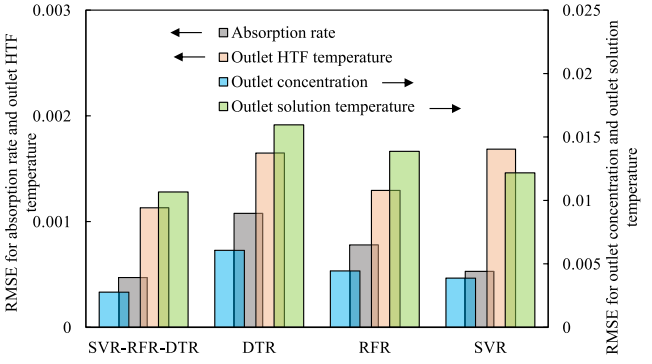

Fig. 7. Effect of combination of SVR, RFR, and DTR on RMSE for the present labels: absorption rate, outlet concentration, solution outlet temperature, and heat transfer fluid outlet temperature.

i) Increasing the chunk number can slightly decrease accuracy since the submodels are trained with a lower number of data.
ii) However, increasing the chunk number decreases the computational time by up to 40 times since the training time for a non-linear regression model, such as support vector regression,

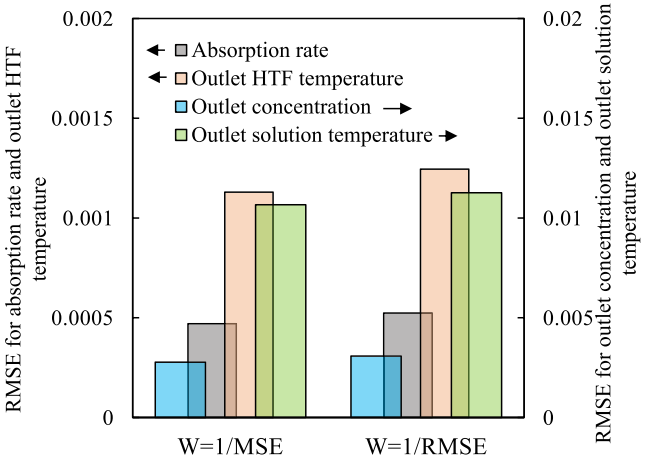

Fig. 8. Effect of using the inverse of MSE and RMSE to calculate the normalized weight for each used regressor to predict the present labels: absorption rate, outlet concentration, solution outlet temperature, and heat transfer fluid outlet temperature.

increases with increasing the number of data due to matrix calculation and memory usage.

iii) The number of data for analysis of chunk number is about 50,000. For a higher number of data, i.e., this dataset (compromising one million data), training the model would be computationally expensive if a low chunk number is considered.

It is worth noting that the computational time is just for training the model. Since the model is trained, the model can be used for designing membrane-based absorbers in less than a few seconds.

Fig. 7 shows the effect of the SVR, RFR, and DTR combination on RMSE for the present labels (output variables) including absorption rate, outlet concentration, solution outlet temperature, and heat transfer fluid outlet temperature. The following can be observed:

i) Combining the models increases accuracy.

ii) SVR-DTR-RFR is the most accurate, and DTR is the least accurate. The reason that aggregating several weak regressors predict the final output more accurately can be attributed to the fact that the models can cover one another weaknesses.

Fig. 8 shows the effect of using the inverse of MSE and RMSE to calculate the normalized weight for each used regressor to predict the present labels including absorption rate, outlet concentration, solution outlet temperature, and heat transfer fluid outlet temperature. Using the inverse of MSE results in a lower RMSE for each label, so MSE was used for calculating the normalized weight in developing the present map-reduce algorithm.

5.2. Prediction of output variables (labels)

At first, the entire dataset is used to train and test the model. 90% of the data is used for training and validation, and 10% for testing. A chunk number of 50 is used to train the model. For SVR, C = 10, epsilon = 0.1, and RBF kernel are used. For RFR, a maximum number of estimators of 200 and a depth of 20 are used. A depth of 1000 is used for DTR. Fig. 9 shows the predicted label (the results of the machine learning-based model) versus the actual label (the results of the numerical modeling) for the four labels including absorption rate, outlet concentration, solution outlet temperature, and heat transfer fluid outlet temperature. The labels can be broadly predicted with an accuracy of 85% or higher, and, more specifically, the following can be observed:

i) The absorption rate can be predicted with an accuracy of 85%; this is the most challenging label to predict since its range is very low ($\sim 10^{-5}$ – 0.025, see Figs. 9 and 10).

ii) Outlet concentration can be predicted with an accuracy of 96%.

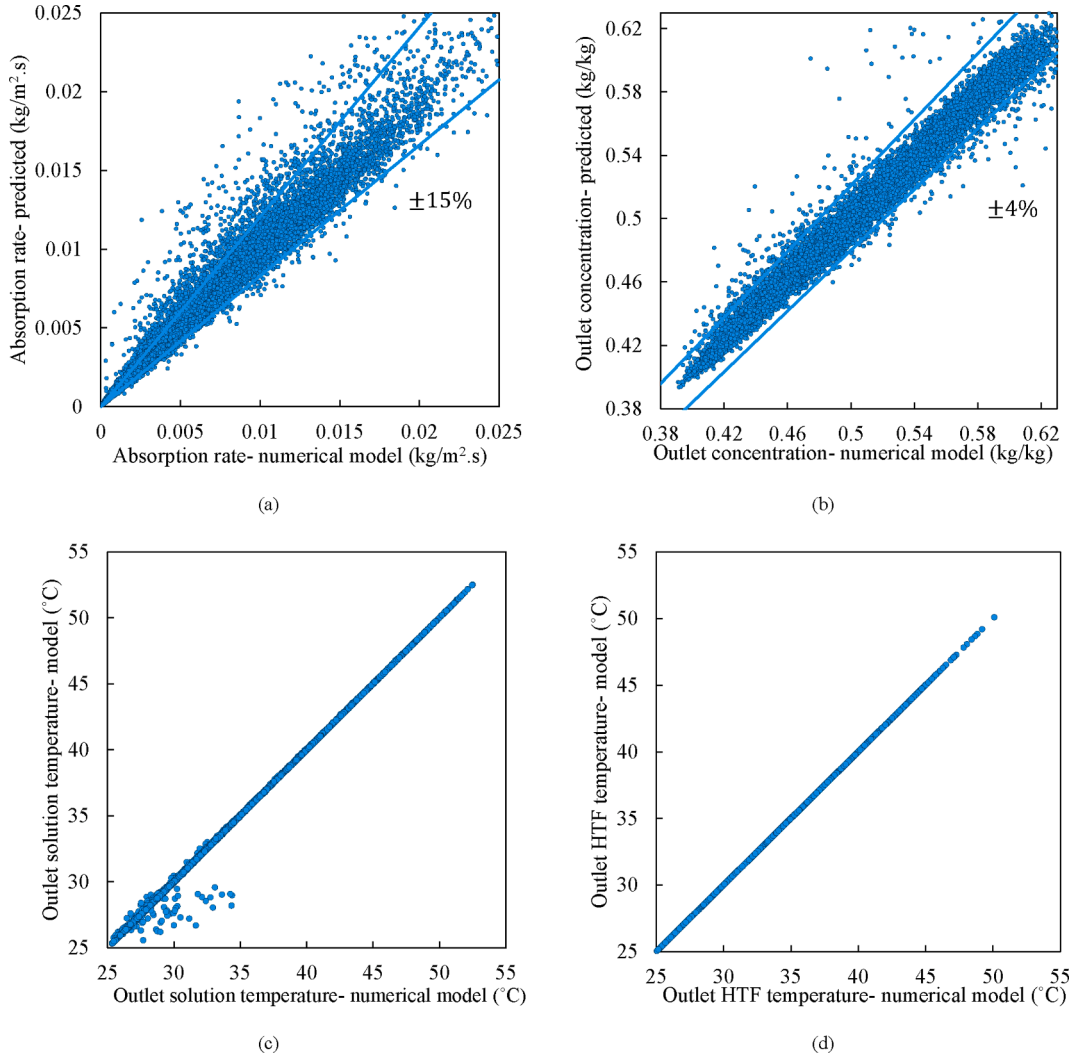

Fig. 9. Predicted label versus actual label based on numerical modeling for the present labels: absorption rate, outlet concentration, solution outlet temperature, and heat transfer fluid outlet temperature. One million data.

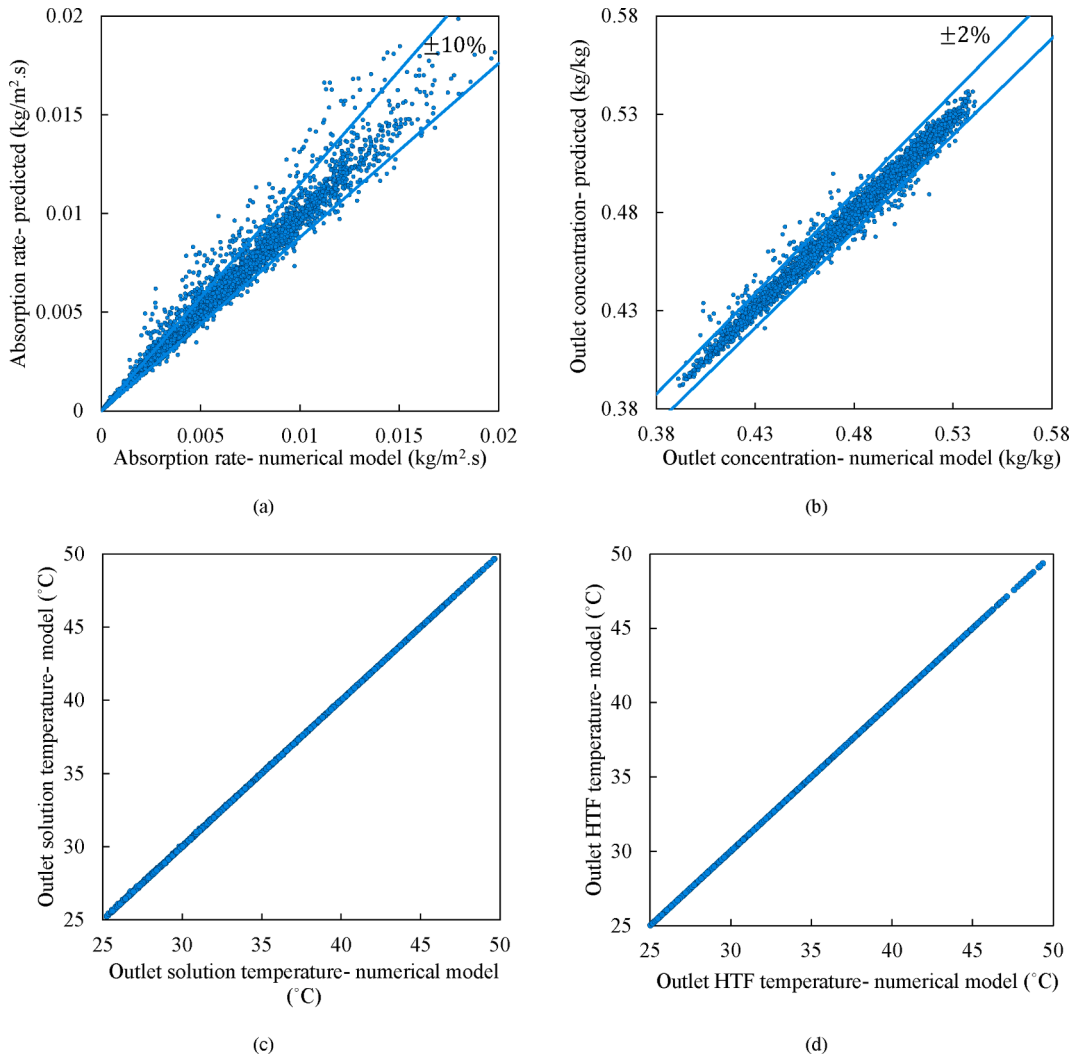

Fig. 10. Predicted label versus actual label based on numerical modeling for the present labels: absorption rate, outlet concentration, solution outlet temperature, and heat transfer fluid outlet temperature. Vapor pressure range of 1.15 to 1.3 kPa (150,000 data points).

iii) Solution outlet temperature and heat transfer fluid outlet temperature can be predicted with an accuracy of 99.5%.

It was shown that the current model could handle one million data points. However, as far as real applications are concerned, the vapor pressure, or evaporator, is known to design a membrane-based absorber. Therefore, to increase the model's accuracy, it is recommended to narrow down the vapor pressure range. For example, for a chiller with an evaporator temperature of 10 ℃, $p_v = 1.227$ kPa, a narrow vapor pressure range of 1.15 to 1.3 kPa can be fed to the model. Fig. 10 shows the predicted label (the results of the machine learning-based model) versus the actual label (the results of the numerical modeling) for the four labels for the vapor pressure range of 1.15 to 1.3 kPa (150,000 data points). As can be seen, by narrowing down the pressure range, the accuracy of the model increases compared to the case that the model is trained with the entire dataset (one million instances).

In conclusion, it was observed that the machine learning-based model can perform with high accuracy. Also, a short period of time is needed to train the model, and the trained model can be used to perform real-time absorber control, optimization, and design in some minutes while the computational time of the numerical modeling can be a barrier for these applications especially optimization and real-time control.

Table 4
Optimized chunk number and hyperparameters for the present model.

Parameter	Entire dataset (one million data)	An arbitrary range of 150 kPa for the vapor pressure
C for SVR	9	32
Epsilon for SVR	0.13	0.07
Number of estimators for RFR	188	292
Depth for RFR	33	49
Depth for DTR	963	1590
Chunk number	57	6

5.3. Hyperparameters optimization

The particle swarm optimization was used to find the optimal chunk number and hyper-parameters to ensure a high accuracy and a low computational time. Table 4 presents the optimized chunk number and hyperparameters for the present model to ensure a high accuracy and a low computational time.

5.4. Validation with experimental data

The model is validated with experimental data from Isfahani et al. [44,45]. As seen in Fig. 11, the machine learning-based model can

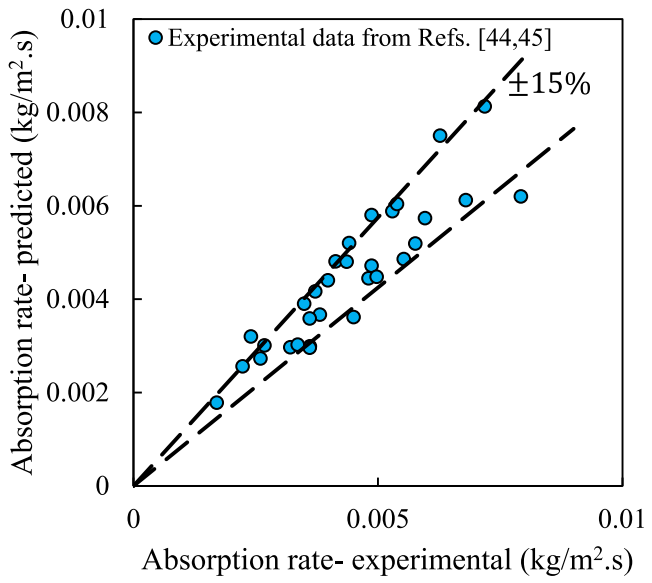

Fig. 11. Validation of present machine learning-based model with experimental data from Refs [44,45].

predict the experimental data, capturing data within a relative difference of 15%.

5.5. *Suggestion for continuing the present work*

Several other regressors and different types of ensembles can be applied to the present dataset. The dataset is available on our GitHub and as supplementary data to this study. Therefore, prospective readers can apply other methods to perform a more accurate prediction compared to the present study.

6. Conclusion

In this study, a novel multi-label, big data-handling machine learning model was proposed for membrane-based absorbers used in absorption heat pumps and chillers. Over one million data points were generated using a 2D finite difference numerical modeling. The dataset consisted of 15 features, input parameters including operating conditions and geometrical parameters, and four labels, output variables including absorption rate, outlet concentration, solution outlet temperature, and heat transfer fluid outlet temperature. Support Vector, Random Forest, and Decision Tree Regressions were combined to develop the present model. A map-reduce algorithm was developed to minimize the computational time. Particle swarm optimization was used to find the optimized hyper-parameters of each model and chunk number. The results of the machine learning-based model were validated with experimental data available in the literature, capturing data within a relative difference of 15%.

The findings of the current research are as follows:

i) RMSE decreases by increasing the number of instances.
ii) Absorption rate is the most challenging label to predict since its range is very low ($\sim 10^{-5}$ – 0.025).
iii) Increasing the chunk number can slightly decrease the accuracy of the model. However, increasing the chunk number decreases the computation time by up to 40 times.
iv) SVR-DTR-RFR is the most accurate model, and DTR is the least accurate.
v) The machine learning-based model can predict the four outputs with an accuracy of over 90%.
vi) The model's accuracy is heightened by training using the desired vapor pressure range.

CRediT authorship contribution statement

Mahyar Ashouri: Conceptualization, Software, Methodology, Investigation, Formal analysis, Data curation, Writing – original draft. **Naghme Kheyrikoochaksarayee:** Conceptualization, Software, Methodology, Investigation, Formal analysis, Data curation, Writing – original draft. **Callum Chhokar:** Methodology, Formal analysis, Investigation, Writing – review & editing. **Amir Shabani:** Supervision, Investigation, Writing – review & editing. **Majid Bahrami:** Supervision, Writing – review & editing, Project administration, Funding acquisition.

Declaration of Competing Interest

The authors declare that they have no known competing financial interests or personal relationships that could have appeared to influence the work reported in this paper.

Data availability

We have shared the dataset and the source code.

Acknowledgments

This research is supported by funding from the Pacific Institute for Climate Solutions (PICS) Opportunity Grant (No. 36170-50280) and the Natural Sciences and Engineering Research Council of Canada (NSERC) Advancing Climate Change Science in Canada Grant (No. 536076-18). We acknowledge the support of the Natural Sciences and Engineering Research Council of Canada (NSERC) Collaborative Research and Training Experience program, CREATE (No. 554770-2021).

Appendix A. Supplementary material

Supplementary data to this article can be found online at https://doi.org/10.1016/j.enconman.2023.117376.

References

[1] Salari A, Ashouri M, Hakkaki-Fard A. On the performance of inclined rooftop solar chimney integrated with photovoltaic module and phase change material: a numerical study. Sol Energy 2020;211:1159–69.
[2] Ashouri M, Hakkaki-Fard A. Improving the performance of the finned absorber inclined rooftop solar chimney combined with composite PCM and PV module. Sol Energy 2021;228:562–74. https://doi.org/10.1016/J.SOLENER.2021.09.088.
[3] Energy Use Data Handbook Tables | National Research Council Government of Canada. Available online: https://oee.nrcan.gc.ca/corporate/statistics/neud/dpa/menus/trends/handbook/tables.cfm .
[4] Yuan Z, Ou X, Peng T, Yan X. Development and application of a life cycle greenhouse gas emission analysis model for mobile air conditioning systems. Appl Energy 2018;221:161–79.
[5] Leibowicz BD, Lanham CM, Brozynski MT, Vázquez-Canteli JR, Castejón NC, Nagy Z. Optimal decarbonization pathways for urban residential building energy services. Appl Energy 2018;230:1311–25.
[6] Winstead C, Bhandari M, Nutaro J, Kuruganti T. Peak load reduction and load shaping in HVAC and refrigeration systems in commercial buildings by using a novel lightweight dynamic priority-based control strategy. Appl Energy 2020;277:115543.
[7] Maiorino A, Del Duca MG, Aprea C. ART. I. CO.(ARTificial Intelligence for COoling): An innovative method for optimizing the control of refrigeration systems based on Artificial Neural Networks. Appl Energy 2022;306:118072.
[8] Mateu-Royo C, Navarro-Esbrí J, Mota-Babiloni A, Molés F, Amat-Albuixech M. Experimental exergy and energy analysis of a novel high-temperature heat pump with scroll compressor for waste heat recovery. Appl Energy 2019;253:113504.
[9] Miró L, Gasia J, Cabeza LF. Thermal energy storage (TES) for industrial waste heat (IWH) recovery: a review. Appl Energy 2016;179:284–301. https://doi.org/10.1016/j.apenergy.2016.06.147.
[10] Huang P, Copertaro B, Zhang X, Shen J, Löfgren I, Rönnelid M, et al. A review of data centers as prosumers in district energy systems: renewable energy integration and waste heat reuse for district heating. Appl Energy 2020;258:114109.

[11] Forman C, Muritala IK, Pardemann R, Meyer B. Estimating the global waste heat potential. Renew Sustain Energy Rev 2016;57:1568–79.
[12] Xu ZY, Wang RZ, Yang C. Perspectives for low-temperature waste heat recovery. Energy 2019;176:1037–43.
[13] Sui Z, Wu W, You T, Zheng Z, Leung M. Performance investigation and enhancement of membrane-contactor microchannel absorber towards compact absorption cooling. Int J Heat Mass Transf 2021;169:120978. https://doi.org/10.1016/J.IJHEATMASSTRANSFER.2021.120978.
[14] Chen L, Ge Y, Qin X, Xie Z. Exergy-based ecological optimization for a four-temperature-level absorption heat pump with heat resistance, heat leakage and internal irreversibility. Int J Heat Mass Transf 2019;129:855–61.
[15] Ashouri M, Elsafi AM, Girnik IS, Bahrami M. An analytical solution for heat and mass transfer in falling film absorption with arbitrary thermal boundary conditions. Appl Therm Eng 2023;231:120891. https://doi.org/10.1016/J.APPLTHERMALENG.2023.120891.
[16] Ali AHH, Schwerdt P. Characteristics of the membrane utilized in a compact absorber for lithium bromide–water absorption chillers. Int J Refrig 2009;32:1886–96.
[17] Venegas M, de Vega M, García-Hernando N, Ruiz-Rivas U. Adiabatic vs non-adiabatic membrane-based rectangular micro-absorbers for H2O-LiBr absorption chillers. Energy 2017;134:757–66. https://doi.org/10.1016/J.ENERGY.2017.06.068.
[18] Ashouri M, Bahrami M. On the absorption rate of membrane-based adiabatic sorber beds: an analytical approach. Int J Heat Mass Transf 2023;209:124105.
[19] Zhai C, Sui Y, Sui Z, Wu W. Ionic liquids for microchannel membrane-based absorption heat pumps: Performance comparison and geometry optimization. Energy Convers Manag 2021;239:114213.
[20] Gao Z, Kumar N, Yang Z, Gluesenkamp K, Abuheiba A, Moghaddam S, et al. Internally cooled membrane-based absorber for dehumidification and water heating: Validated model and simulation study. Energy Convers Manag 2021;230:113787.
[21] Ye B, Wang Z, Yan X, Chen G. Performance analysis of a variable-stage open absorption heat pump combined with a membrane absorber. Energy Convers Manag 2019;184:290–300.
[22] de Vega M, Venegas M, García-Hernando N. Viability on the desorption and air condensation of water in a compact membrane-based microchannel desorber-condenser for cooling applications. Energy Convers Manag 2022;267:115919.
[23] Jafarian H, Sayyaadi H, Torabi F. Numerical modeling and comparative study of different membrane-based liquid desiccant dehumidifiers. Energy Convers Manag 2019;184:735–47.
[24] Shafieian A, Khiadani M. A novel solar-driven direct contact membrane-based water desalination system. Energy Convers Manag 2019;199:112055.
[25] Ali AHH. Design of a compact absorber with a hydrophobic membrane contactor at the liquid–vapor interface for lithium bromide–water absorption chillers. Appl Energy 2010;87:1112–21.
[26] Ashouri M, Bahrami M. Heat and mass transfer in laminar falling film absorption: a compact analytical model. Int J Heat Mass Transf 2022;188:122598.
[27] Meyer T, Ziegler F. Analytical solution for combined heat and mass transfer in laminar falling film absorption using first type boundary conditions at the interface. Int J Heat Mass Transf 2014;73:141–51.
[28] Elsafi AM, Ashouri M, Bahrami M. A similarity solution for laminar forced convection heat transfer from solid spheres. Int J Heat Mass Transf 2022;196:123310.
[29] Yu D, Chung J, Moghaddam S. Parametric study of water vapor absorption into a constrained thin film of lithium bromide solution. Int J Heat Mass Transf 2012;55:5687–95. https://doi.org/10.1016/J.IJHEATMASSTRANSFER.2012.05.064.
[30] Asfand F, Stiriba Y, Bourouis M. CFD simulation to investigate heat and mass transfer processes in a membrane-based absorber for water-LiBr absorption cooling systems. Energy 2015;91:517–30. https://doi.org/10.1016/J.ENERGY.2015.08.018.
[31] Woods J, Pellegrino J, Kozubal E, Burch J. Design and experimental characterization of a membrane-based absorption heat pump. J Memb Sci 2011;378:85–94.
[32] Abdollahi F, Hashemifard SA, Khosravi A, Matsuura T. Heat and mass transfer modeling of an energy efficient hybrid membrane-based air conditioning system for humid climates. J Memb Sci 2021;625:119179.
[33] Sui Z, Zhai C, Wu W. Swirling flow for performance improvement of a microchannel membrane-based absorber with discrete inclined grooves. Int J Refrig 2021.
[34] Venegas M, De Vega M, García-Hernando N. Parametric study of operating and design variables on the performance of a membrane-based absorber. Appl Therm Eng 2016;98:409–19.
[35] Sui Z, Sui Y, Wu W. Multi-objective optimization of a microchannel membrane-based absorber with inclined grooves based on CFD and machine learning. Energy 2022;240:122809.
[36] Sui Y, Zhai C, Wu W, Leung MKH. Multi-scale computer-aided molecular design of ionic liquid for absorption heat transformer based on machine learning. Energy Convers Manag 2022;261:115617.
[37] Sui Z, Wu W. AI-assisted maldistribution minimization of membrane-based heat/mass exchangers for compact absorption cooling. Energy 2022;125922.
[38] Ashouri M, Bahrami M. Analytical solution for coupled heat and mass transfer in membrane-based absorbers. Int J Heat Mass Transf 2022;192:122892.
[39] Incropera FP, DeWitt DP. Fundamentals of heat and mass transfer. John Wiley & Sons New York 1996. https://doi.org/10.1016/j.applthermaleng.2011.03.022.
[40] Asfand F, Stiriba Y, Bourouis M. Performance evaluation of membrane-based absorbers employing H2O/(LiBr+ LiI+ LiNO3+ LiCl) and H2O/(LiNO3+ KNO3+ NaNO3) as working pairs in absorption cooling systems. Energy 2016;115:781–90.
[41] Mason EA. EA M, AP M. Gas transportin porous media: The dusty-gas model; 1983.
[42] Florides GA, Kalogirou SA, Tassou SA, Wrobel LC. Design and construction of a LiBr–water absorption machine. Energy Convers Manag 2003;44:2483–508.
[43] Home Page | Digital Research Alliance of Canada n.d. https://alliancecan.ca/en (accessed December 20, 2022).
[44] Isfahani RN, Sampath K, Moghaddam S. Nanofibrous membrane-based absorption refrigeration system. Int J Refrig 2013;36:2297–307.
[45] Isfahani RN, Moghaddam S. Absorption characteristics of lithium bromide (LiBr) solution constrained by superhydrophobic nanofibrous structures. Int J Heat Mass Transf 2013;63:82–90.
[46] De Vega M, García-Hernando N, Venegas M. Experimental performance of membrane water absorption in LiBr solution with and without cooling. Appl Therm Eng 2020;180:115786.
[47] Bhagwat R, Schmid M, Moghaddam S. Experimental and numerical analysis of a three-fluid membrane-based ionic liquid desiccant absorber. Int J Heat Mass Transf 2022;183:122122.
[48] Harrou F, Saidi A, Sun Y. Wind power prediction using bootstrap aggregating trees approach to enabling sustainable wind power integration in a smart grid. Energy Convers Manag 2019;201:112077.
[49] Javanmard ME, Ghaderi SF, Hoseinzadeh M. Data mining with 12 machine learning algorithms for predict costs and carbon dioxide emission in integrated energy-water optimization model in buildings. Energy Convers Manag 2021;238:114153.
[50] Hong W-C. Chaotic particle swarm optimization algorithm in a support vector regression electric load forecasting model. Energy Convers Manag 2009;50:105–17.
[51] Mohammadi K, Shamshirband S, Anisi MH, Alam KA, Petković D. Support vector regression based prediction of global solar radiation on a horizontal surface. Energy Convers Manag 2015;91:433–41.
[52] Sun H, Gui D, Yan B, Liu Y, Liao W, Zhu Y, et al. Assessing the potential of random forest method for estimating solar radiation using air pollution index. Energy Convers Manag 2016;119:121–9.
[53] Ibrahim IA, Khatib T. A novel hybrid model for hourly global solar radiation prediction using random forests technique and firefly algorithm. Energy Convers Manag 2017;138:413–25.
[54] Abubaker AM, Ahmad AD, Singh BB, Akafuah NK, Saito K. Multi-objective linear-regression-based optimization of a hybrid solar-gas turbine combined cycle with absorption inlet-air cooling unit. Energy Convers Manag 2021;240:114266.
[55] Piloto-Rodríguez R, Sánchez-Borroto Y, Lapuerta M, Goyos-Pérez L, Verhelst S. Prediction of the cetane number of biodiesel using artificial neural networks and multiple linear regression. Energy Convers Manag 2013;65:255–61.
[56] Kavzoglu T, Sahin EK, Colkesen I. Landslide susceptibility mapping using GIS-based multi-criteria decision analysis, support vector machines, and logistic regression. Landslides 2014;11:425–39.
[57] Liu Y, Guo B, Zou X, Li Y, Shi S. Machine learning assisted materials design and discovery for rechargeable batteries. Energy Storage Mater 2020;31:434–50.
[58] Hundi P, Shahsavari R. Comparative studies among machine learning models for performance estimation and health monitoring of thermal power plants. Appl Energy 2020;265:114775.
[59] Dalton A, Bekker B. Exogenous atmospheric variables as wind speed predictors in machine learning. Appl Energy 2022;319:119257.
[60] Khatibi T, Kheyrikoochaksarayee N, Sepehri MM. Analysis of big data for prediction of provider-initiated preterm birth and spontaneous premature deliveries and ranking the predictive features. Arch Gynecol Obstet 2019;300:1565–82.
[61] Poli R, Kennedy J, Blackwell T. Particle swarm optimization: an overview. Swarm Intell 2007;1:33–57.